NONLINEAR PROCESSES IN MULTI-MODE OPTICAL FIBERS

by

Hamed Pourbeyram Kaleibar

A Thesis Submitted in

Partial Fulfillment of the

Requirements for the Degree of

Master of Science

in Engineering

at

The University of Wisconsin-Milwaukee

May 2014

ABSTRACT
NONLINEAR PROCESSES IN MULTI-MODE OPTICAL FIBERS

by

Hamed Pourbeyram Kaleibar

The University of Wisconsin-Milwaukee, 2014
Under the Supervision of Professor Arash Mafi

Nonlinear processes in optical fibers can affect data transmission and power carried by optical fibers and can limit the bandwidth and the capacity of optical communications. On the other hand nonlinear phenomena could be utilized to build in-fiber all-optical light sources and amplifiers. In this thesis new peaks inside an optical fiber have been generated using nonlinear processes. An intense green pump laser has been launched into a short fiber and specific modes have been excited to generate two new peaks in red and blue wavelengths, where two pump photons are annihilated to create two new photons in red and blue. The generated peaks are shifted far from pump; therefore they are less polluted by pump and Raman induced noises. The phase matching condition and the photon-flux rate for spontaneous and stimulated FWM have been studied both theoretically and experimentally for a commercial grade SMF-28 fiber. In low power and spontaneous regime new peaks are generated from quantum vacuum noise. Using the same pump laser for a long fiber, up to 21 new peaks spanning from green to Infrared have been generated. These peaks are equally spaced by 13THz. Generation of a Raman cascade spanning the wavelength range of 523 to 1750 nm wavelength range, in a standard telecommunication graded-index multimode optical fiber has been reported. Despite the highly multimode nature of the pump, the Raman peaks are generated in specific modes of the fiber, confirming substantial beam cleanup during the stimulated Raman scattering process.

Dedicated to my beloved parents and Wife

TABLE OF CONTENTS

LIST OF FIGURES

ACKNOWLEDGMENTS

I would like to express my gratitude towards many individuals whose help and assistance made it possible for me to accomplish this work. First, I deeply thank Professor Arash Mafi, who gave me the opportunity to work on this project. Without his perpetual mentorship, patience, support and invaluable inspiration, I would have not been able to establish the comprehension and understanding of my research. I would like to thank my committee members Professors George Hanson, Chiu Law and Guangwu Xu for their time and valuable suggestions. I would like to thank Professor Gowind P. Agrawal from the Institute of Optics at University of Rochester for his great comment and helps. I would like to thank Dr. Steven Hardcastle for the SEM images. I would like to thank Dr. Elham Nazemosadat for her patience in answering my questions and kind help in conducting this research especially in Four-Wave-Mixing theory. I would like to thank National Science Foundation for providing the financial support under grant number 1253233 . I would like to thank all of my labmates Dr. Elham Nazemosadat, Dr. Salman Karbasi Valashani, Dr. Parisa Gandomkar Yarandi, Seyed Rasoul Hosseini, Ryan Frazier, Joel Michael Kolata, Christopher Storms for making a positive atmosphere in our lab over the period of my stay at the Photonics research group. I would like to thank all my friends for all the good times that we had in Milwaukee. I would like to thank my wife Fahimeh for all her support and understandings that helped me focus on my work far away from my family. Last but not least, I would like to thank my beloved parents, Jamileh and Ebadolah, my brother, Saeed and my sister, Hajar, for their unreserved love and uplifting motivations while I was thousands of kilometers away from them.

Chapter 1

Introduction

1.1 Optical Fibers

Total Internal Reflection (TIR) happens when a wave is incident from a medium with a lower refractive index to a medium with a higher refractive index and the incident angle is larger than "Critical angle". The total internal reflection is the main phenomenon responsible for the transmission of light through an optical fiber. The first uncladded glass fibers were fabricated in 1920s using this phenomenon. However born of fiber optics field could be considered in 1950s when by using a cladded layer considerable improvement was achieved in the quality of the optical fibers [1].

Fiber optic communication was not used practically for several years and until mid-1950 virtually all communication systems relied on the transmission of information over electrical cables or radio-frequency and microwave electromagnetic radiation propagation in free space.

One of the early issues was high losses in light transmission for long distances, because light unlike radio frequency waves gets absorbed easily in an opaque medium like fog or clouds. In 1970, by fabricating fibers from low-loss silica, this issue was resolved [2]. Nowadays lightwave communication is the preferred technology in many applications,

because of its enormous transmission capacity, distant spacing of repeaters, and immunity from electromagnetic interference (EMI).

Optical fibers act like a waveguide for light. A multi-mode fiber is a waveguide that supports many modes and a single-mode fiber supports only a single mode. multi-mode fibers usually have larger core diameters and are used for short distance communication and high power transmission.

1.2 Nonlinear Processes in Optical Fibers

Throughout the long history of optics, and indeed until relatively recently it was thought that all optical media were linear, and that their optical properties were independent of light intensity. However, more recently it was observed that optical media can show nonlinear behavior in the presence of high intensity light. The presence of an optical field modifies the properties of the medium, which in turn could cause changes in the light passing through it. Nonlinearity is related to the medium in which light is propagating through, and not the light itself. Hence, it is the nonlinear medium which makes the interaction of light with light possible.

The beginning of nonlinear optics could be considered 1961, when for the first time a Ruby laser was used to generate the second harmonic radiation inside a crystal [12]. Later, with the availability of low-loss optical fibers in the 1970s, investigation of nonlinear effects in optical fibers became feasible, and for the first time Raman and Brillouin scattering inside an optical fiber were studied. [3]. Soon after, other nonlinear phenomena such as four-mixing were studied as well. [4].

1.3 Motivation for This Work and Outline of Dissertation

Several features such as small core size and long interaction length make optical fibers a desired nonlinear media. In the early years of fiber optics, the main focus was on single-mode optical fibers and multi-mode fibers were considered an undesired medium for optical communication and nonlinear optics. However, with the recent advances in technology and the need for higher data capacity, there has been a growing interest in multi-mode fibers. It has been estimated that the single-mode fiber in a few decades will reach it's maximum capacity which naturally will lead to use of multi-mode fibers as a way to increase capacity per fiber [5].

Although, the core diameter of a multi-mode fiber is larger than that of a single mode fiber, light still remains mostly intense in the the center of the fiber [6]. Moreover, the presence of several modes in a multi-mode fiber and the interaction between them makes this fiber a suitable medium for nonlinear processes. The need for a better understanding of these processes inside a multimode optical fiber encouraged us to conduct this research and investigate the nonlinear behavior in the presence of many modes.

Chapter 2

Four-Wave-Mixing in Multi-Mode Fibers

2.1 Theoretical Study

2.1.1 Origin of Four-wave-Mixing

Maxwell's equations are the equations governing the propagation of an electromagnetic field in a medium. In the international system of units and considering a medium in the absence of free charges and currents such as optical fibers ($J = 0,\ \rho_f = 0$) these equations take the form of:

$$\nabla \times \mathbf{E} = -\frac{\partial \mathbf{B}}{\partial t}, \tag{2.1}$$

$$\nabla \times \mathbf{H} = \frac{\partial \mathbf{D}}{\partial t}, \tag{2.2}$$

$$\nabla.\mathbf{D} = \mathbf{0}, \tag{2.3}$$

$$\nabla.\mathbf{B} = \mathbf{0}, \tag{2.4}$$

where $\mathbf{E}$ and $\mathbf{B}$ are electric and magnetic field vectors, and $\mathbf{D}$ and $\mathbf{B}$ are corresponding electric and magnetic flux densities.

The flux densities $\mathbf{D}$ and $\mathbf{B}$ arise in response to the electric and magnetic fields propagating inside the medium and are related to them through constitutive relations given by:

$$\mathbf{D} = \epsilon_\mathbf{0}\mathbf{E} + \mathbf{P} \tag{2.5}$$

$$\mathbf{H} = \mu_\mathbf{0}(\mathbf{H} + \mathbf{M}) \tag{2.6}$$

where ϵ_0 is the vacuum permitivity, μ_0 is the vacuum permeability and $\mathbf{P}$ and $\mathbf{M}$ are induced electric and magnetic polarizations. For nonmagnetic medium such as optical fiber, $\mathbf{M} = \mathbf{0}$.

Wave equation that describes light propagation in optical fibers can be obtained using Maxwell's equations, by eliminating $\mathbf{B}$ and $\mathbf{D}$:

$$\nabla \times \nabla \times \mathbf{E} = -\frac{1}{c^2}\frac{\partial^2 \mathbf{E}}{\partial t^2} - \mu_0 \frac{\partial^2 \mathbf{P}}{\partial t^2}. \tag{2.7}$$

The origin of FWM lies in the nonlinear response of a bound electron of a material to an electromagnetic field. This induces a polarization in the medium containing terms related to the linear and nonlinear susceptibilities

$$\mathbf{P} = \epsilon_\mathbf{0}\Big(\chi(\mathbf{1}) : \mathbf{E} + \chi(\mathbf{2}) : \mathbf{EE} + \chi(\mathbf{3}) : \mathbf{EEE}\Big). \tag{2.8}$$

In the equation above $\chi(1)$ is the linear polarization, and $\chi(2)$ is the second-order susceptibility which is the source of nonlinear behaviors such as second-harmonic generation and sum-frequency generation. Last term, $\chi(3)$, is third-order susceptibility and is responsible for phenomena such as third-harmonic generation, nonlinear refrac-

tion and four-wave-mixing. In an isotropic medium the second-order susceptibility vanishes, so second-order nonlinear processes do not occur in silica fibers. The third-order susceptibility is responsible for processes involving nonlinear interactions among four optical waves and includes such phenomena as Raman Scattering, four-wave-mixing, and third-harmonic generation. Hence, the nonlinear polarization induced in a fiber can be understood from a third-order polarization term in Eq. 2.8 [7]:

$$\mathbf{P_{NL}} = \epsilon_{\mathbf{0}} \chi(\mathbf{3}) : \mathbf{EEE}, \tag{2.9}$$

In general, FWM is a polarization dependent process and requires a full vectorial study. However, in most cases conducting a scalar study will give reasonable answers. For CW waves oscillating at frequencies ω_j and linearly polarized along the same axis the total electric field can be written as

$$\mathbf{E} = \frac{\mathbf{1}}{\mathbf{2}} \sum_{\mathbf{j}} \mathbf{E_j} \ \mathbf{exp}[\mathbf{i}(\beta_{\mathbf{j}}\mathbf{z} - \omega_{\mathbf{j}}\mathbf{t})] + \mathbf{c.c.}, \tag{2.10}$$

where indices j show different frequency components of the electric field and $\beta_j = \tilde{n}_j \omega_j / c$ is the propagation constant and $\tilde{n}_j$ is the mode index.

2.1.2 Coupled Amplitude Equations

Degenerate FWM transfers energy from a strong pump wave to two waves, upshifted and down shifted in frequency from pump frequency ω_p, known as Stokes and anti-Stokes beams. Equation 2.10 is substituted in the wave equation 2.7, assuming quasi-CW conditions in which time dependence of the field components E_j can be neglected.

By integrating over spatial mode profiles, the evolution of the amplitude $A_j(z)$ can be represented by coupled amplitude equations:

$$\partial_z A_p = \frac{in_2(\omega_p)\omega_p}{c}[(\eta_{pp}|A_s|^2 + 2\sum_{k=a,s}\eta_{pk}|A_k|^2)A_p + \eta_{ppsa}A_sA_aA_p^*e^{-i\Delta kz}] \tag{2.11a}$$

$$\partial_z A_s = \frac{in_2(\omega_s)\omega_s}{c}[(\eta_{ss}|A_s|^2 + 2\sum_{k=p,s}\eta_{sk}|A_k|^2)A_s + \eta_{sapp}A_p^2A_a^*e^{i\Delta kz}] \tag{2.11b}$$

$$\partial_z A_a = \frac{in_2(\omega_a)\omega_a}{c}[(\eta_{aa}|A_a|^2 + 2\sum_{k=p,a}\eta_{ak}|A_k|^2)A_a + \eta_{aspp}A_p^2A_s^*e^{i\Delta kz}], \tag{2.11c}$$

where spatial dependence of electric field is given by $E_j(r) = F_j(x,y)A_j(z)$. Using undepleted pump approximation in which pump amplitude A_p is strong than those of Stokes A_s and anti-Stokes A_a beams the pump evolution equation will be:

$$\partial_z A_p = \frac{in_2(\omega_p)\omega_p}{c}\eta_{pp}P_0^pA_p \tag{2.12}$$

which can be solved independent of the other two equations and will give :

$$A_p(z) = \sqrt{P_0^p}e^{i\varphi_p}\exp(i\gamma_{pp}P_0^pz) \tag{2.13}$$

where P_0^p is the pump power and φ_p is the phase of pump and

$$\gamma_{pp} = \frac{n_2(\omega_p)\omega_p}{c}\eta_{pppp} \qquad (\text{Note} : \eta_{\text{pppp}} = \eta_{\text{pp}}) \tag{2.14}$$

These equation could be solved classically and solution could be found. However it become useful to consider a quantum approach and replace A_s and A_a with quantum operator $\hat{A}_s$ and $\hat{A}_a$ which satisfies commutation relation:

$$[\hat{A}_i(z,\tau), \hat{A}_j^\dagger(z,\tau')] = \delta_{ij}\delta(\tau-\tau') \qquad j,k = x,y \tag{2.15}$$

Under the undepleted-pump approximation the differential equations governing the generation and propagation of the Stokes A_s at frequency ω_s and anti-Stokes A_a at frequency ω_a in the presence of a strong pump field A_p at frequency ω_p are given by:

$$\begin{aligned}\partial_z \hat{A}_s &= 2i\gamma_{ps}|A_p|^2\hat{A}_s + i\gamma_{sa}A_p^2\hat{A}_a^* e^{i\Delta\beta z} \\ \partial_z \hat{A}_a &= 2i\gamma_{pa}|A_p|^2\hat{A}_a + i\gamma_{as}A_p^2\hat{A}_s^* e^{i\Delta\beta z}\end{aligned} \tag{2.17}$$

Here A_p have been considered as a classical field while $\hat{A}_i$ $(i = a, s)$ is a quantum operator. The nonlinear coefficients in Eqs. 2.16 are given by

$$\begin{aligned}\gamma_{ps} &= \frac{n_2(\omega_s)\ \omega_s}{c}\eta_{spps}, \quad \gamma_{sa} = \frac{n_2(\omega_s)\ \omega_s}{c}\eta_{spap}, \\ \gamma_{pa} &= \frac{n_2(\omega_a)\ \omega_a}{c}\eta_{appa}, \quad \gamma_{as} = \frac{n_2(\omega_a)\ \omega_a}{c}\eta_{apsp},\end{aligned} \tag{2.18}$$

$$\eta_{ijkl} = \int d^2x\ F_i^* F_j F_k^* F_l, \quad i, j, k, l \in \{p, s, a\}, \tag{2.19}$$

where F_p, F_s, and F_a are the mode field profiles evaluated at ω_p, ω_s, and ω_a, respectively, and the nonlinear index coefficient n_2 is evaluated at the respective frequencies. c is the speed of light in vacuum, and each mode field profile is assumed to be normalized to unity, i.e. $\int d^2x\ |F_i|^2 = 1$.

The pump, Stokes, and anti-Stokes fields each in general can belong to different spatial modes of the optical fiber, as long as they satisfy energy and momentum conservation. By using a 523nm light as the input, only few modes will be excited in the fiber and only some of suitable modes in output will carry substantial amount of power.

The general solutions of Eqs. 2.16 can be expressed as

$$A_s(z) = A_s(0)\Big[\cosh(gz) + i\frac{\kappa}{2g}\sinh(gz)\Big]e^{i\phi_s} \tag{2.20a}$$
$$+ A_a^*(0)\Big[i\frac{\gamma_{sa}P_p^0}{g}\sinh(gz)\Big]e^{2i\varphi_p}e^{i\phi_s},$$
$$A_a(z) = A_a(0)\Big[\cosh(gz) + i\frac{\kappa}{2g}\sinh(gz)\Big]e^{i\phi_a} \tag{2.20b}$$
$$+ A_s^*(0)\Big[i\frac{\gamma_{as}P_p^0}{g}\sinh(gz)\Big]e^{2i\varphi_p}e^{i\phi_a},$$

where

$$\phi_s = 2\gamma_{ps}P_p z + \kappa z/2, \tag{2.21a}$$
$$\phi_a = 2\gamma_{pa}P_p z + \kappa z/2, \tag{2.21b}$$

and

$$g = \sqrt{\Big(\tilde{\gamma}_1 P_p^0\Big)^2 - \Big(\kappa/2\Big)^2}, \tag{2.22a}$$
$$\kappa = 2\tilde{\gamma}_2 P_p^0 - \Delta\beta, \tag{2.22b}$$
$$\tilde{\gamma}_1 = \sqrt{\gamma_{sa}\gamma_{as}}, \tag{2.22c}$$
$$\tilde{\gamma}_2 = \gamma_{ps} + \gamma_{ps} - \gamma_{pp}. \tag{2.22d}$$

2.1.3 Phase Matching

To generate four wave mixing in a fiber necessary condition of phase-matching can be satisfied which could be done by various methods such as divided-pump process, birefringence matching, near zero-dispersion wavelength matching, and phase matching using different fiber modes [8]. Focus of this work is on the last type while using a single laser pump configuration. For single pump configuration both pump photons are traveling at the same frequancy, and as a result it has been shown that there will be large shift between signal and pump frequency compared to all other cases of phase matching, as was first observed by C. Lin in 1981 [9]. The advantage of this method is being less affected by Raman Scattering, so the generated signal will be far away from Raman noise and won't be polluted by it, which will lead to a naturally pure source of entangled photons. $\Delta\beta$ is the phase mismatch between the pump, Stokes, and anti-Stokes fields and is given by

$$\Delta\beta = 2\beta_p(\omega_p) - \beta_a(\omega_a) - \beta_s(\omega_s), \tag{2.23}$$

where $\beta_p(\omega_p)$, $\beta_s(\omega_s)$, $\beta_a(\omega_a)$ are the propagation constants of the pump, stokes, and anti-stokes modes at frequencies ω_p, ω_s and ω_a respectively. Equation 2.23 can be approximated by the Taylor expansion up to the first order in Ω around ω_p as

$$\Delta\beta(\Omega) = \delta\beta^{(0)} + \delta\beta^{(1)}\Omega - \bar{\beta}^{(2)}\Omega^2 \tag{2.24}$$

where

$$(2\pi c)\Omega = \omega_p - \omega_s = \omega_a - \omega_p, \tag{2.25a}$$

$$\delta\beta^{(0)} = 2\beta_p(\omega_p) - \beta_a(\omega_p) - \beta_s(\omega_p), \tag{2.25b}$$

$$\delta\beta^{(1)} = (2\pi c)\Big(\beta_s^{(1)}(\omega_p) - \beta_a^{(1)}(\omega_p)\Big), \tag{2.25c}$$

$$\bar{\beta}^{(2)} = (2\pi c)^2\frac{1}{2}\Big(\beta_s^{(2)}(\omega_p) + \beta_a^{(2)}(\omega_p)\Big), \tag{2.25d}$$

where equation 2.25a is a result of momentum conservation and the following definition has been used:

$$\beta_i^{(n)}(\omega) = \partial_\omega^{(n)}\beta_i(\omega), \quad i \in \{p, s, a\}. \tag{2.26}$$

For the SMF-28 fiber, linear phase matching can be achieved when the pump mode is in the LP_{01} mode. In Fig. 2.1, the linear phase matching condition can be shown by $\Delta\beta(\Omega) = 0$ as the intersection of $\bar{\beta}^{(2)}\Omega^2$ plotted as a function of Ω in a blue dashed parabola, and $\delta\beta^{(0)} + \delta\beta^{(1)}\Omega$ plotted in a red solid line. The horizontal axis Ω in Fig. 2.1 is the spectral separation of the LP_{01} mode from the pump with the other mode being in LP_{02}. Therefore, the linearly phase-matched intersection point at $\Omega \approx 3285$ cm^{-1} corresponds to the anti-Stokes (Stokes) in the LP_{01} (LP_{02}) mode, while the intersection at $\Omega \approx -2961$ cm^{-1} corresponds to the anti-Stokes (Stokes) in the LP_{02} (LP_{01}) mode.

The numerical values of the parameter describing the phase-matched frequencies are $\delta\beta^{(0)} \approx 231.1$ cm^{-1}, $\delta\beta^{(1)} \approx 7.84 \times 10^{-3}$, and $\bar{\beta}^{(2)} \approx 2.37 \times 10^{-5}$ cm. The linear phase-matching spectral shifts can be approximated to the first order by

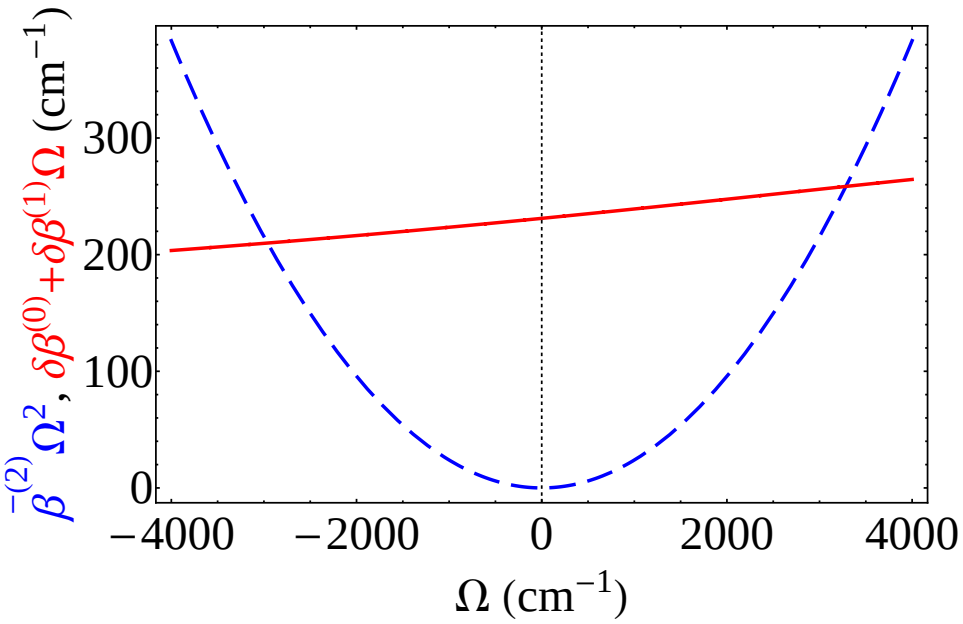

Figure 2.1: Phase-Matching for FWM. Dashed blue curve shows nonlinear part and solid black line shows linear part of phase matching

$$\Omega_{\rm pm}^{\rm L} = \pm\sqrt{\frac{\delta\beta^{(0)}}{\bar{\beta}^{(2)}}} + \frac{\delta\beta^{(1)}}{2\bar{\beta}^{(2)}}. \tag{2.27}$$

It should pointed out that in SMF-28, the $\bar{\beta}^{(2)}$ in Eq. 2.25d can be accurately described by only the chromatic dispersion and the waveguiding contribution to its value can be ignored in the phase-matching process, as has also been verified numerically. Therefore, one can write

$$\bar{\beta}^{(2)} \approx \lambda_p D_p, \text{ where } D_p = -(2\pi)^{-1}\lambda^2\partial_\lambda^2 n(\lambda)|_{\lambda_p}. \tag{2.28}$$

This approximation results in in less than 1% deviation from the exact value with $\bar{\beta}^{(2)} \approx 2.39 \times 10^{-5}$ cm.

The maximum gain is obtained at the nonlinear phase-matching point $\Omega_{\rm pm}^{\rm NL}$ which is

approximately given by

$$\Omega_{\mathrm{pm}}^{\mathrm{NL}} = \pm\sqrt{\frac{\delta\beta^{(0)} - 2\tilde{\gamma}_2 P_p^0}{\bar{\beta}^{(2)}}} + \frac{\delta\beta^{(1)}}{2\bar{\beta}^{(2)}} \tag{2.29}$$

The maximum gain value is $g_{\max} = \tilde{\gamma}_1 P_p^0$. Relation between pump frequency and shifted frequencies are

$$\omega_a = \omega_p + (2\pi c)\Omega_{\mathrm{pm}}^{\mathrm{NL}} \tag{2.30}$$

$$\omega_s = \omega_p - (2\pi c)\Omega_{\mathrm{pm}}^{\mathrm{NL}}. \tag{2.31}$$

Around the phase-matching point, the gain can be reliably approximated as

$$g = g_{\max}\sqrt{1 - (\tilde{\Omega}/\tilde{\Omega}_0)^2} \tag{2.32}$$

where

$$\tilde{\Omega}_0 = \frac{\tilde{\gamma}_1 P_p^0}{|\delta\beta^{(1)}/2 - \bar{\beta}^{(2)}\Omega_{\mathrm{pm}}^{\mathrm{NL}}|} \tag{2.33}$$

Using Eq. 2.27, $\tilde{\Omega}_0$ can be reliably approximated as

$$\tilde{\Omega}_0 \approx \frac{\tilde{\gamma}_1 P_p^0}{\sqrt{\bar{\beta}^{(2)} \delta\beta^{(0)}}} \tag{2.34}$$

To adjust numerical calculation with experimental result, values used for fiber core radius and index difference are slightly different from what we found in data sheet. This could be resulted from some unknown features usually found in commercial optical fibers. In figure 2.2 index difference and fiber core radius size for a specific stokes wavelength has been shown. Each graph shows a specific stokes beam at wavelength and LP_{02} mode.

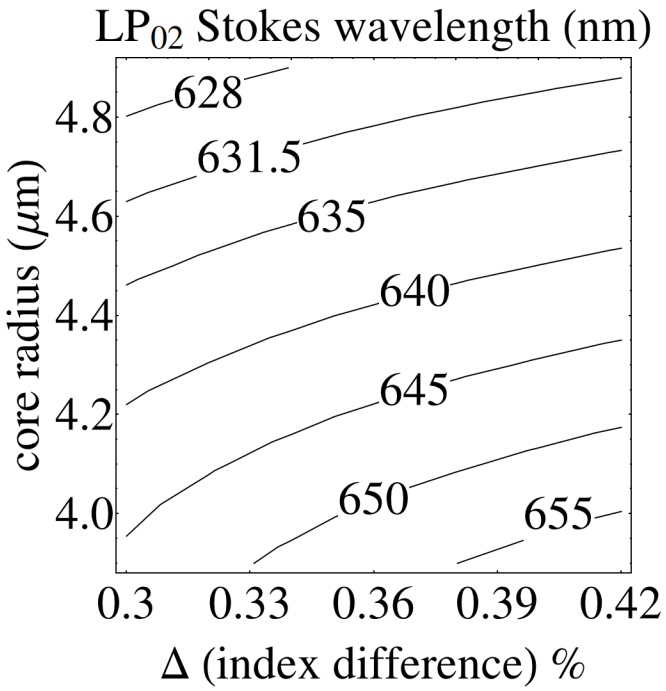

Figure 2.2: Core radius and index difference for different stokes wavelengths from 628nm to 650nm

2.1.4 Signal Power versus Pump Power

In spontaneous FWM where there is no injected light at Stokes and anti-Stokes are generated from vacuum noise which is basically a quantum effect [10]. Photon generation in Stokes wavelength is:

$$I_u \equiv < \hat{A}_u^{\dagger}(L,\tau), \hat{A}_u(L,\tau) > \tag{2.35}$$

where index $u = s$ is for Stokes, $u = a$ for anti-Stokes and brackets denote average with respect to vacuum input state and a thermally populated photon reservoir [10]. The Stokes photon flux (According to Ref. [10]) is given by

$$\begin{aligned}
I_s &= c \int d\tilde{\Omega} \left(\frac{\gamma_{sa} P_p^0}{g}\right)^2 \sinh^2(gz) \qquad (2.36)\\
I_s &= c\,(\gamma_{sa} P_p^0 z)^2 \int d\tilde{\Omega} \left(\frac{\sinh(gz)}{gz}\right)^2 \\
I_s &= c\,\tilde{\Omega}_0 (\gamma_{sa} P_p^0 z)^2 \int dx \left(\frac{\sinh(g_{\max} z\sqrt{1-x^2})}{g_{\max} z\sqrt{1-x^2}}\right)^2 \\
I_s &= c\,\frac{\tilde{\Omega}_0}{g_{\max}^2} (\gamma_{sa} P_p^0)^2 \int dx\, \frac{\sinh^2(g_{\max} z\sqrt{1-x^2})}{1-x^2} \\
I_s &= c \left(\frac{\gamma_{sa}}{\gamma_{as}}\right) \tilde{\Omega}_0\, \Pi(g_{\max} z),
\end{aligned}$$

The anti-Stokes photon flux is similarly given by

$$I_a = c \left(\frac{\gamma_{as}}{\gamma_{sa}}\right) \tilde{\Omega}_0 \, \Pi(g_{\max} z), \tag{2.37}$$

Here, it have been defined by

$$\Pi(y) = \int dx \, \frac{\sinh^2(y\sqrt{1-x^2})}{1-x^2}. \tag{2.38}$$

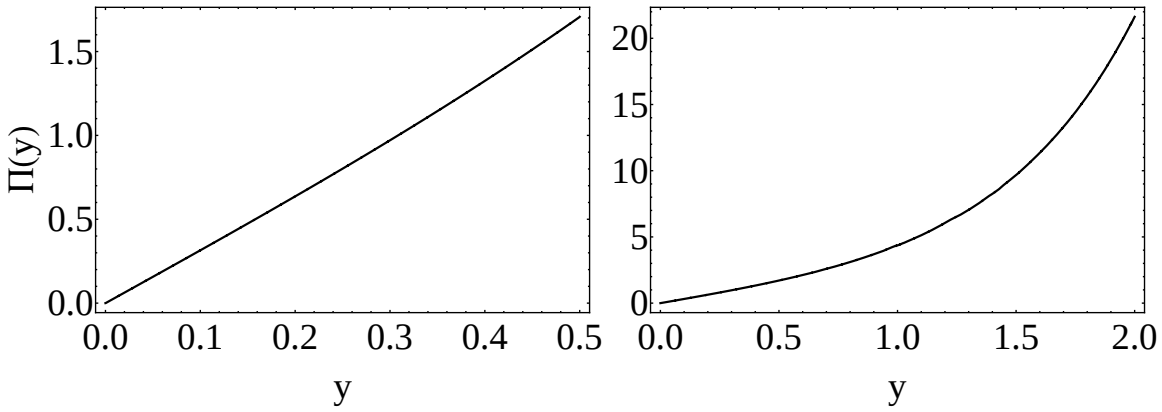

Figure 2.3: The Π function. For small y it act like a linear function and for large y like a hyperbolic sine.

Now by using Eq. 2.34 and Eq. 2.28 the photon flux at Stokes and anti-Stokes frequencies could be expressed as

$$I_s \approx c \left(\frac{\gamma_{sa}}{\gamma_{as}}\right) \frac{g_{\max}}{\sqrt{\lambda_p D_p \delta\beta^{(0)}}} \, \Pi(g_{\max} z) \tag{2.39}$$

$$I_a \approx c \left(\frac{\gamma_{as}}{\gamma_{sa}}\right) \frac{g_{\max}}{\sqrt{\lambda_p D_p \delta\beta^{(0)}}} \, \Pi(g_{\max} z) \tag{2.40}$$

Therefore, the photon flux is proportional to $g_{\max}$ as it should be. However, it is

inversely proportional to $\delta\beta^{(0)}$ which signifies the mode-level separation at the pump wavelength. In other words, $\delta\beta^{(0)}$ shows how different the effective indexes of the modes are at the pump wavelength. Another very rough approximation is

$$\sqrt{\bar{\beta}^{(2)}\delta\beta^{(0)}} \approx \bar{\beta}^{(2)}\Omega_{\mathrm{pm}} \tag{2.41}$$

Therefore, although a rough approximation but good for building intuition could be

$$I_s \approx c \left(\frac{\gamma_{sa}}{\gamma_{as}}\right) \frac{g_{\max}}{\lambda_p D_p \Omega_{\mathrm{pm}}} \Pi(g_{\max} z) \tag{2.42}$$

Therefore, the photon flux is inversely proportional to the spectral separation of the Stokes and anti-Stokes from the pump. The pump is assumed to be a Gaussian pulse in time in the form

$$P_p^0 = \frac{E_p}{\sqrt{\pi\tau_0^2}} \exp\left(-\frac{\tau^2}{\tau_0^2}\right), \tag{2.43}$$

where E_p is the pump pulse energy. The pump pulses used in the experiment are nearly 8 ns long, therefore, it is reasonable to assume a very slowly varying envelope approximation and assume the dispersive terms do not affect the pump power envelope. Total Stokes energy for a given pump pulse cycle can be calculated as

$$
\begin{aligned}
E_s &= \hbar\omega_s \int_{-\infty}^{\infty} d\tau \; I_s \\
&= \hbar\omega_s \int_{-\infty}^{\infty} d\tau \; c \; \left(\frac{\gamma_{sa}}{\gamma_{as}}\right) \; \tilde{\Omega}_0 \; \Pi(g_{\max} z) \\
&\approx \hbar\omega_s \int_{-\infty}^{\infty} d\tau \; c \; \left(\frac{\gamma_{sa}}{\gamma_{as}}\right) \; \frac{\tilde{\gamma}_1 P_p^0}{\sqrt{\bar{\beta}^{(2)}\delta\beta^{(0)}}} \; \Pi(\tilde{\gamma}_1 P_p^0 L) \\
&\approx \frac{\hbar\omega_s c\tau_0}{L\sqrt{\bar{\beta}^{(2)}\delta\beta^{(0)}}} \; \left(\frac{\gamma_{sa}}{\gamma_{as}}\right) \; \int_{-\infty}^{\infty} dy \; \tilde{\gamma}_1 \frac{E_p}{\sqrt{\pi\tau_0^2}} L e^{-y^2} \; \Pi(\tilde{\gamma}_1 \frac{E_p}{\sqrt{\pi\tau_0^2}} L e^{-y^2}) \\
&\approx \left(\frac{\gamma_{sa}}{\gamma_{as}}\right) \; \frac{\hbar\omega_s c\tau_0}{L\sqrt{\bar{\beta}^{(2)}\delta\beta^{(0)}}} \Psi(\tilde{\gamma}_1 \frac{E_p}{\sqrt{\pi\tau_0^2}} L)
\end{aligned}
\tag{2.44}
$$

where it have been defined

$$
\begin{aligned}
\Psi(z_0) &= \int_{-\infty}^{\infty} dy \; z_0 e^{-y^2} \Pi(z_0 e^{-y^2}) \\
&= \iint dx dy \; z_0 e^{-y^2} \frac{\sinh^2(z_0 e^{-y^2}\sqrt{1-x^2})}{1-x^2}.
\end{aligned}
\tag{2.45}
$$

Using the method of steepest descent, it possible to show that

$$
\Pi(y) \approx \frac{\sqrt{\pi}}{4} \frac{\exp(2y)}{\sqrt{y}}, \quad y \gg 1. \tag{2.46}
$$

Another important approximation needed is

$$
\int_{-\infty}^{\infty} dx \; \sqrt{y e^{-x^2}} \; \exp(y e^{-x^2}) = \sqrt{\pi} e^y, \quad y = 1. \tag{2.47}
$$

Therefore, it could be written

$$\Psi(z_0) \approx \frac{\pi}{4\sqrt{2}} \exp(2z_0), \quad z_0 \gg 1. \tag{2.48}$$

Therefore, the Stokes pulse energy is given by

$$E_s \approx \left(\frac{\gamma_{sa}}{\gamma_{as}}\right) \left(\frac{\pi}{\sqrt{32\bar{\beta}^{(2)}\delta\beta^{(0)}}}\right) \left(\frac{c\tau_0}{L}\right) \hbar\omega_s \exp\left(2\tilde{\gamma}_1 \frac{E_p}{\sqrt{\pi\tau_0^2}} L\right) \tag{2.49}$$

For our experiment $(\bar{\beta}^{(2)}\delta\beta^{(0)})^{-1/2} \approx 13.51$. Using $n_2 = 2.2 \times 10^{-16}$ cm^2/W, It could be calculated that $\tilde{\gamma}_1 = 3.05$/W.km and $\tilde{\gamma}_2 = 4.88$/W.km.

2.2 Experimental Results

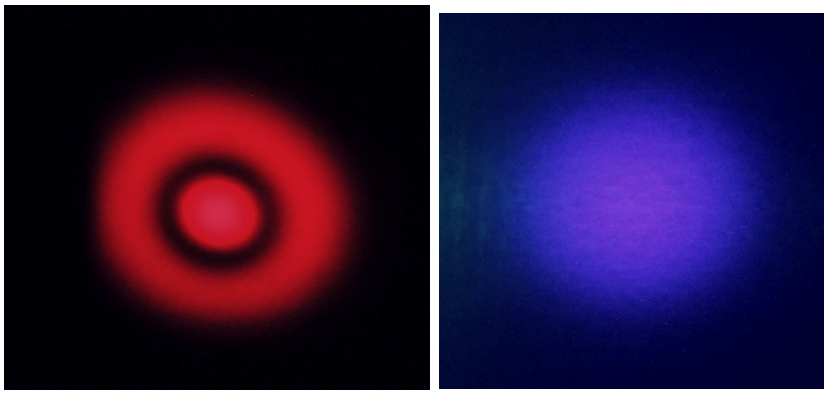

Figure 2.4: Signal (left) and Idler (right) of FWM generated in SMF-28

Experimental setup includes a 523nm frequency doubled Nd:YLF laser with 8 ns pulse duration and Repetition rate of 100Hz. Output of this laser is launched into a short (10-50cm) SMF-28 fiber. Core radius of the fiber is 8.2μm and output power of the

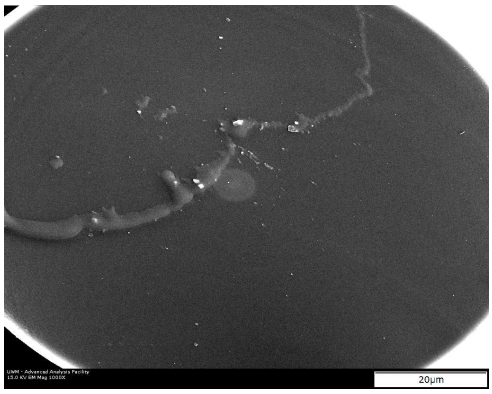

Figure 2.5: SEM image of SMF-28 used in experiment

laser is around hundreds of Kwatts. By properly exciting the fiber modes and coupling enough power into the fiber anti-Stoke and Stokes peaks at blue (446.5 nm) and Red (631.5 nm) have been observed, as shown in figure 2.6.

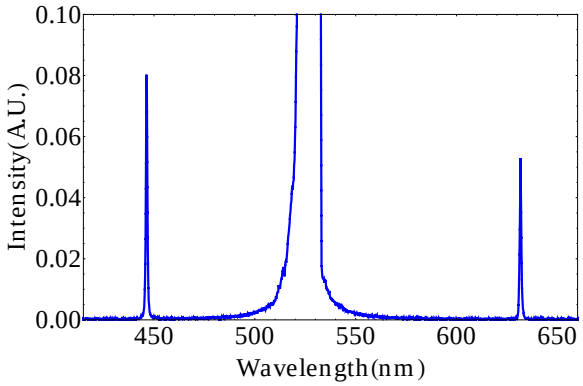

Figure 2.6: Measured spectrum of generated Stokes and anti-Stokes by FWM

Since the fiber is short no significant Raman peaks have been detected in the experiment. Only for fibers longer than 30cm and at high powers there was a small peak of Raman in 532nm. Figure 2.7 shows the Raman peak observed for a 30cm fiber. In this figure the detection was optimized to observe maximum Raman signal.

The observed anti-stoke peak was in red and it's mode was mostly like LP_{02} mode. As expected, four wave mixing occurs with a large shift to pump for a single-mode Pump (two pumps at same frequency) [11], and almost only the fundamental mode of

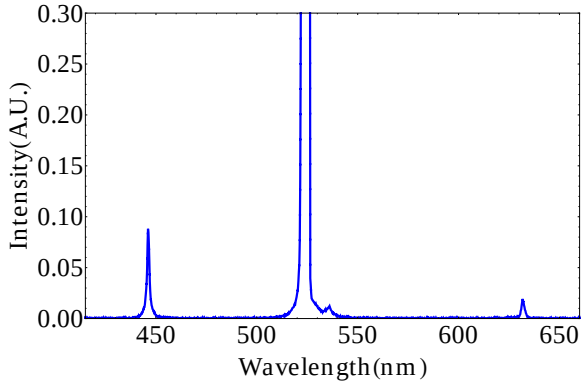

Figure 2.7: Beside FWM, Raman gets generated in longer fibers. Small peak near pump at around 532 shows Raman peak gets generated for a 30cm fiber

the fiber (LP_{01}) gets excited.

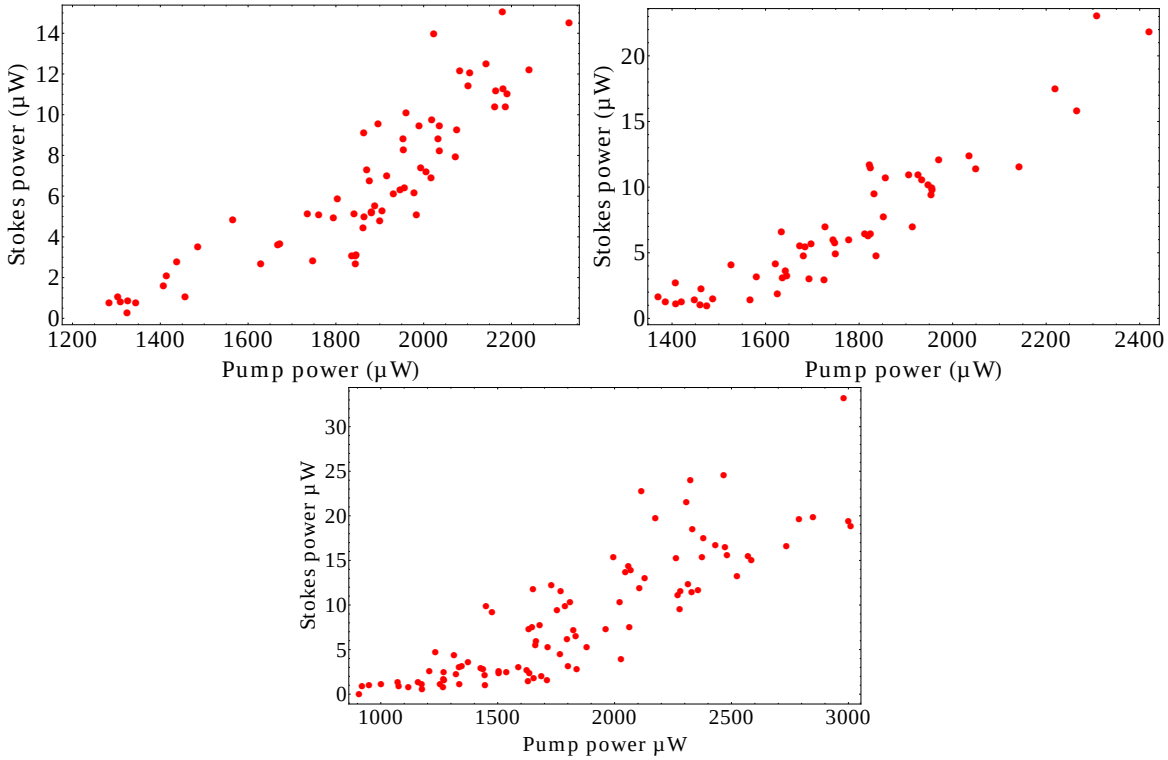

Figure 2.8: Stokes power beam as a function of pump power

Output of a FWM process is sensitive to the modes which are excited inside the fiber. Hence, one needs to excite the proper modes to observe favored output. As shown

in figure 2.4, experimental results show a Stokes at LP_{02} and an anti-Stokes at LP_{01} generated by a pump in LP_{01} mode. These images are the outputs of 15cm of the SMF-28.

2.3 Discussion

In this section FWM in a SMF-28 has been investigated both theoretically and experimentally. An approximate theoretical formula for photon flux in a SMF-28 fiber has been introduced. Also, the intensity of the stokes beam as a function of pump power has been experimentally investigated. Although experimental and theoretical results show the same behavior, numerically they do not match perfectly and for an measured pump power, the theoretical estimate for the Stokes power is lower than the value observed in the experiment.

In Fig. 2.10 result of experimental data and theoretical calculations have been shown, in which dashed blue line shows theoretical calculation and blue dots show experimental data and red line show line fitted to experimental data. For 15cm and 30cm slopes are identical while for 50cm slopes for experimental and theoretical results does not match. Investigation of parameters affecting the generation of Stokes and anti-Stokes beam could be as a future study to show how experiment and theory match.

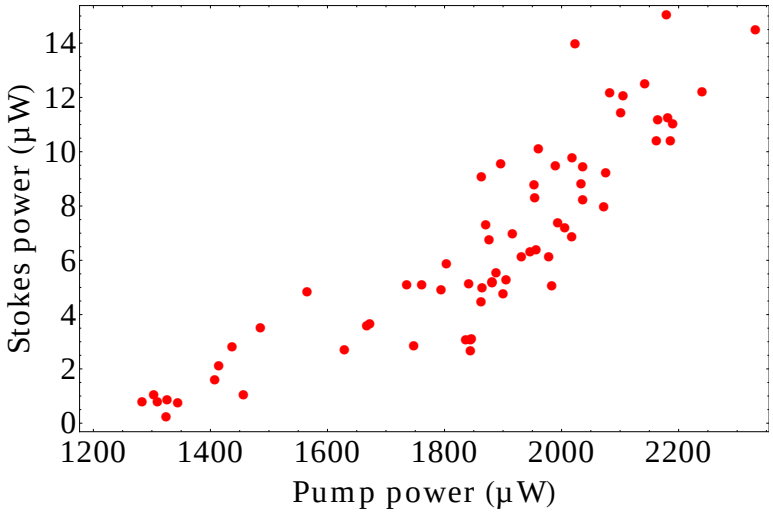

(a) 15cm

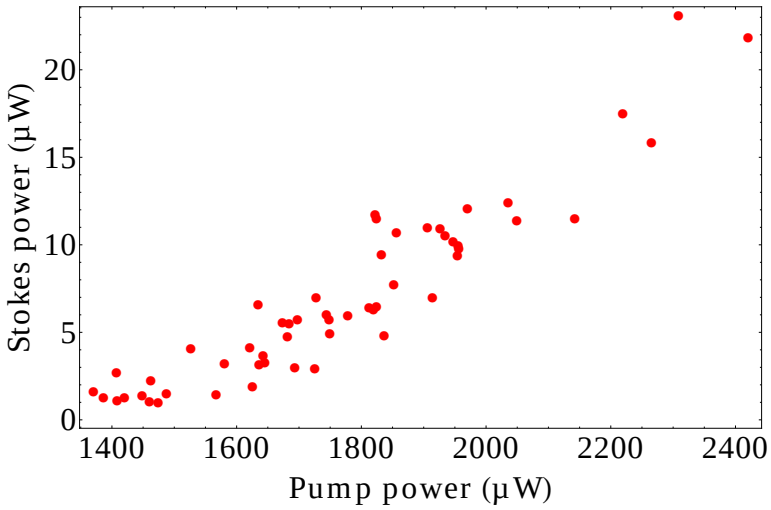

(b) 30cm

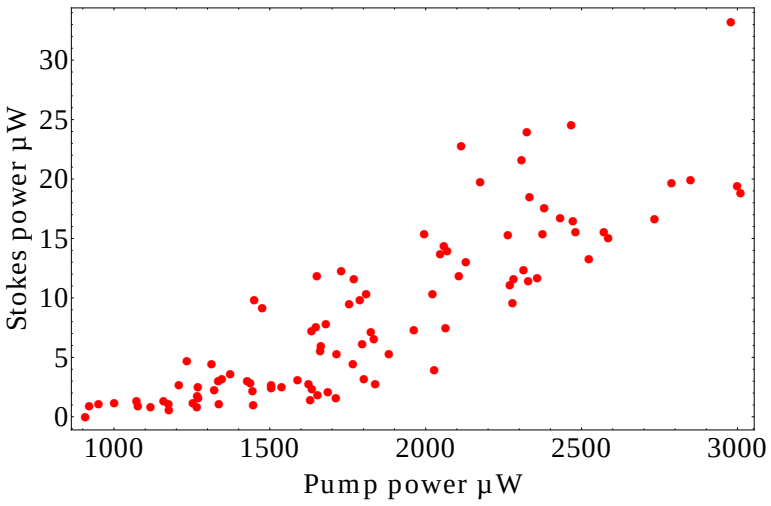

(c) 50cm

Figure 2.9: Logarithmic plot of experimental measurements for signal energy versus pump power in (a) 15 cm, (b) 30cm and (c) 50cm of a SMF-28 fiber.

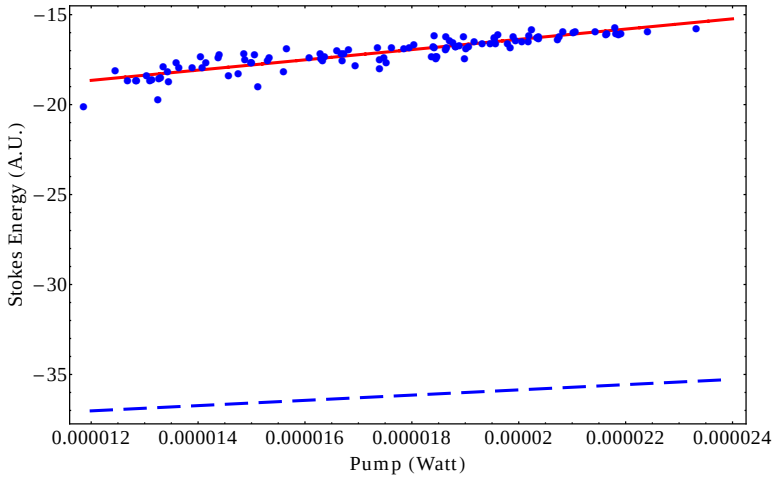

(a) 15cm

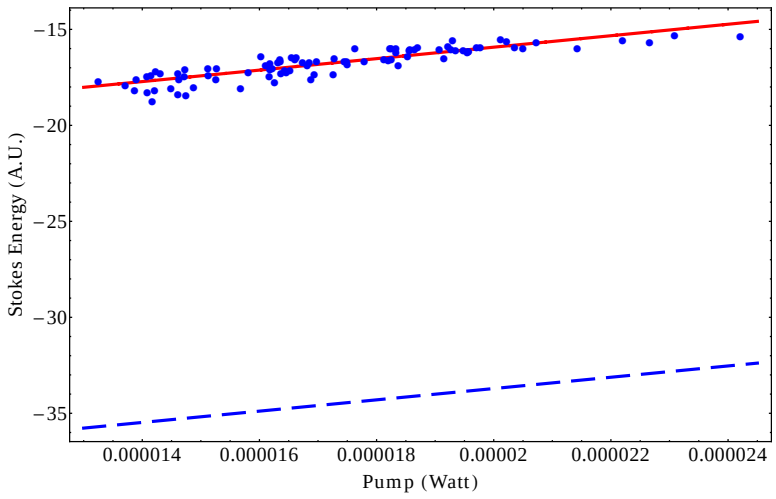

(b) 30cm

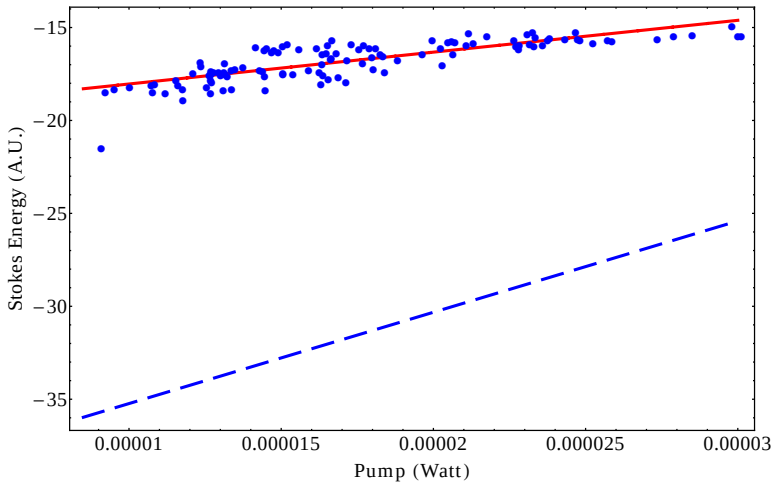

(c) 50cm

Figure 2.10: Logarithmic plot of theoretical and experimental data for signal energy versus pump power in (a) 15 cm, (b) 30cm and (c) 50cm of a SMF-28 fiber.

Chapter 3

Raman Scattering in Multi-Mode Fibers

3.1 Introduction

Stimulated Raman scattering (SRS) is a well-known nonlinear process with numerous applications including optical amplifiers, tunable lasers, spectroscopy, meteorology, and optical coherence tomography. SRS was first observed in silica glass fibers in 1972 by Stolen et al. [13]. They used a frequency-doubled, pulsed, Nd:YAG laser operating at the 532 nm wavelength to pump a single-mode optical fiber and observed Stokes emission at 545 nm. Since then, several groups have reported the observation of SRS in optical fibers using various configurations [15–18]. Cohen and Lin [15] generated 6 cascaded Raman peaks in a silica fiber, pumped by a mode-locked, Q-switched, Nd:YAG laser operating at 1064 nm. Rosman [16] observed 15 orders of cascaded Raman peaks by pumping a silica fiber at 532 nm with a frequency-doubled Nd:YAG laser. Other configurations involving unconventional fibers have been used for extreme Raman-comb generation. For example, Couny et al. [18] demonstrated the generation of a Raman comb spanning wavelengths from 325 nm to 2300 nm in a

1m-long hydrogen-filled hollow-core photonic crystal fiber.

In this part generation of new wavelengths, mediated by the SRS process, in a standard graded-index multimode fiber (GIMF) have been studied. The GIMF is pumped at a wavelength of 523 nm, and a cascade of optical-frequency Raman peaks is generated on the Stokes side of the pump. At high power levels the measured spectrum extends up to 1750 nm, which is the upper detection limit of experimental instruments have been used which is an optical spectrum analyzer (OSA). The generation of such a wide wavelength range, extending from 523 to 1750 nm, using a large-core telecommunication-grade multimode fiber which have been done distinguishes results reported in this thesis from those carried out in small-core or highly customized optical fibers [19].

Multimode optical fibers are easy to handle and are also easy to align to external sources; however, their large core diameter is perceived as undesirable for nonlinear applications. Despite a lower effective nonlinearity associated with a larger core of conventional multimode fibers, the multimode nature of these fibers can play an important role in some nonlinear applications. In particular, the presence of multiple propagating modes with different dispersive properties results in expanded phase-matching opportunities for the generation of four-wave mixing (FWM) signals in optical fibers [7, 14, 17, 20]. The GIMF used in our experiments has two desirable properties that make it particularly suitable for SRS generation. First, because the effective modal area of each mode in the GIMF scales only as square root of the core area, the effective nonlinearity of some propagating modes is comparable with conventional single-mode fibers [6]. Second, a relatively high GeO_2 content in the core of the standard telecommunication GIMF used in experiments results in a higher peak Raman gain coefficient compared with silica-core fibers [21].

3.2 Generation of New Wavelengths and Spectral Measurements

The pump have been used in experiment is a frequency-doubled, Q-switched, Nd:YLF laser operating at 523 nm wavelength, and its 8-ns duration pulses are coupled to the input tip of the fiber using a microscope objective. The laser beam is not diffraction-limited, and many modes in the fiber are excited simultaneously. The GIMF is a 1-km long standard, 50/125-μm, bare fiber (Corning ClearCurve OM2). The output spectrum is measured using a CCS200 spectrometer (from Thorlabs) operating in the range of 200–1000 nm and a MS9740A OSA (from Anritsu) covering the 600–1750 nm wavelength range. Energy of input pulses required for reaching the Raman threshold have been measured immediately after coupling into the fiber (less then 1-meter of propagation inside the GIMF) to be 20.9 μJ; estimated peak power is to be about 2.5 kW. The pulse energy decreased to about 0.515 μJ after 1-km of propagation, which is consistent with the expected attenuation of about 16 dB/km at the pump wavelength. The measured threshold power for the first Raman peak (P_0^{cr}) is consistent with $g_R P_0^{cr} L_{\text{eff}} \approx 16 A_{\text{eff}}$ [7] using the effective length of $L_{\text{eff}} = 270$ m (considering the 16 dB/km attenuation), $g_R \approx 2.9 \times 10^{-13}$ m/W (at 523 nm wavelength and considering the GeO_2 doping), and an effective area of $A_{\text{eff}} = \pi \times (62.5\ \mu\text{m})^2$ (considering the heavily multimode and overfilling nature of the pump).

The sequential generation of cascaded Raman peaks is initiated by the pump at 523 nm. As the pump power is increased, the first Stokes line extracts power from the pump until it becomes strong enough to seed the generation of next Stokes line. This process continues and more and more Raman peaks gets generated with increasing pump power. The 20 cascaded peaks shown in Fig. 3.1(a) extend from 523 nm to just

above 1000 nm in wavelength. The estimated input peak power of pump pulses used in the experiment is 22 kW for this figure.

As the pump power is further increased, even more cascaded Raman peaks appear beyond the 1000 nm wavelength range of spectrometer. Figure 3.1(b) shows the spectrum measured with the Anritsu OSA in the range of 900–1750 nm at the maximum pump power level (just below the burning threshold of fiber's input tip). It is necessary to stress that the two plots in Figs. 3.1(a) and 3.1(b) should not be compared directly because they correspond to different power levels and employ different vertical scales. The spectral dip at around 1300 nm and the broad peak beyond 1400 nm are two notable features in this infrared range. The appearance of the spectral dip centered at the 1320-nm wavelength is related to a reduction in the SRS gain occurring near the zero-dispersion-wavelength (ZDW) of the GIMF, where the SRS gain is suppressed due to a near-perfect phase-matching of the FWM process [22,23]. The dip at 1320 nm can be seen more clearly in Fig. 3.2, where the data have been plotted in Fig. 3.1(b) on a logarithmic power scale.

In our opinion, the broad peak centered at 1600 nm results from the onset of modulation instability in the presence of anomalous dispersion. The resulting short pulses can experience Raman-induced spectral shifts as well as collision-based spectral broadening, resulting in a broad supercontinuum-like feature [24, 25]. The generation of the longer wavelengths beyond the ZDW is a very complex phenomenon and is heavily influenced by parametric processes. Even in the absence of perfect phase matching, FWM can seed higher-order Raman waves that are subsequently amplified through SRS [26, 27].

The presence of efficient FWM phase-matching opportunities in the GIMF impacts considerably the generation of the cascaded Raman peaks. Figure 3.3 shows the spec-

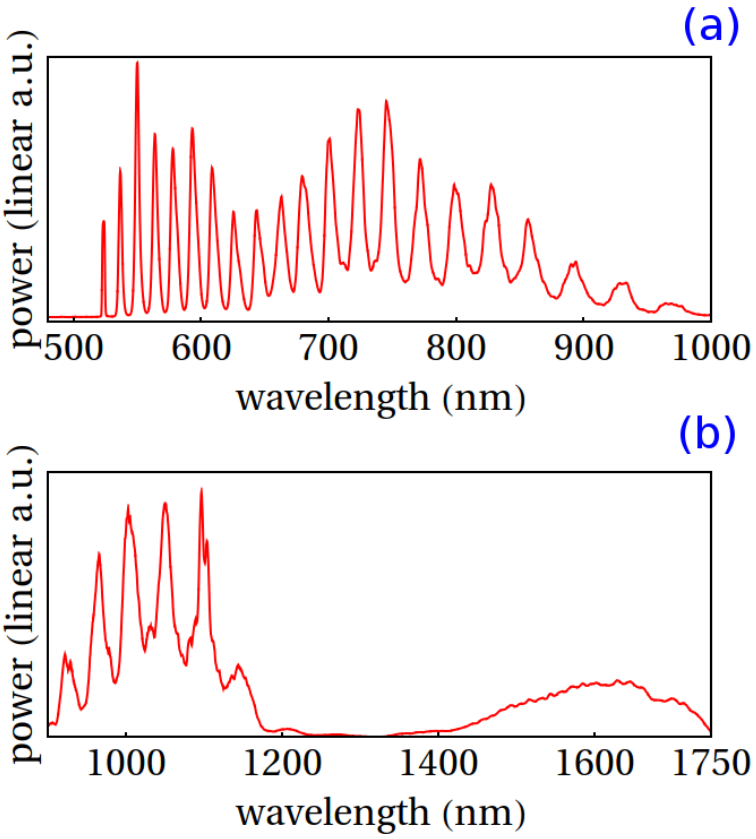

Figure 3.1: (a) Cascaded Raman peaks measured with the spectrometer. (b) Spectrum measured by the OSA when pump power is increased to just below the burning threshold of fiber's tip; the spectral dip at around 1300 nm and the broad peak beyond 1400 nm are two notable features in this infrared range.

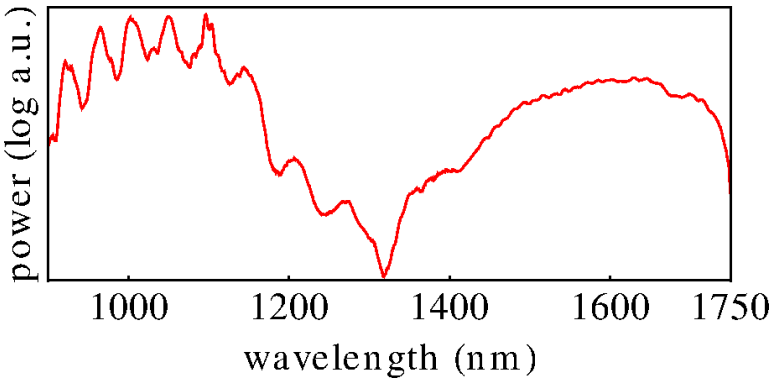

Figure 3.2: Same as Fig. 3.1(b) but data plotted using a logarithmic vertical scale. The input pump power is just below the burning threshold of fiber's tip.

trometer data in the frequency domain, by plotting on the horizontal axis the frequency shift of the Raman comb relative to the pump frequency, and power on a logarith-

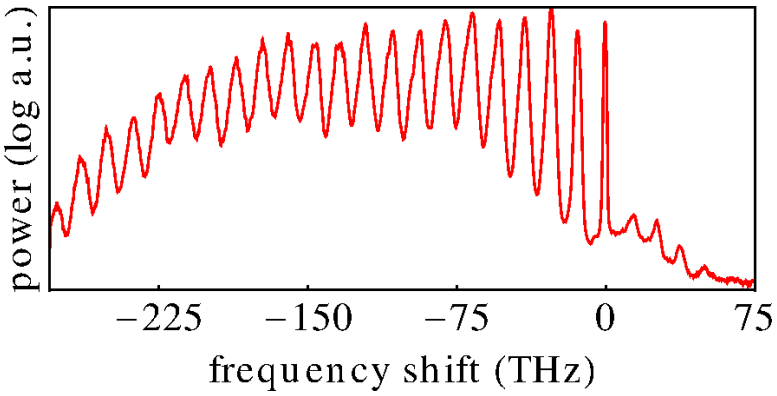

Figure 3.3: Cascaded Raman peaks measured with the spectrometer and plotted using frequency shift on the horizontal axis. Notice the presence of FWM peaks on the anti-Stokes side.

mic scale on the vertical axis. Equal spacing of various peaks on the Stokes side is expected for a cascaded Raman process. However, the presence of FWM frequencies on the anti-Stokes side of the pump is the most notable feature in this figure. The phase-matched frequency counterparts of these FWM idlers on the Stokes side can affect the location and amplitude of the cascaded Raman peaks. In this experiment it have been observed that the strength of the FWM signal depended on launch conditions, and FWM was absent (or highly suppressed) in some of the measurements. The highly multimode nature of the pump made it very difficult to find the optimum launch position for the generation of the anti-Stokes peaks; It needed to scan the input pump beam over the fiber core to find the point at which the anti-Stokes peaks appeared with considerable power.

In order to explore the effect of FWM on the SRS peaks, an offset in the input pump beam used by $\approx 15\ \mu m$ from the center of the fiber core . The pump now excites the GIMF modes with different power ratios, resulting in efficient FWM in a different set of phase-matched wavelengths. The result is a shift in the position of the spectral combs. The red and green spectra in Fig. 3.4 are measured before and after offsetting the pump laser, respectively. The shift seems to be seeded around the third cascaded

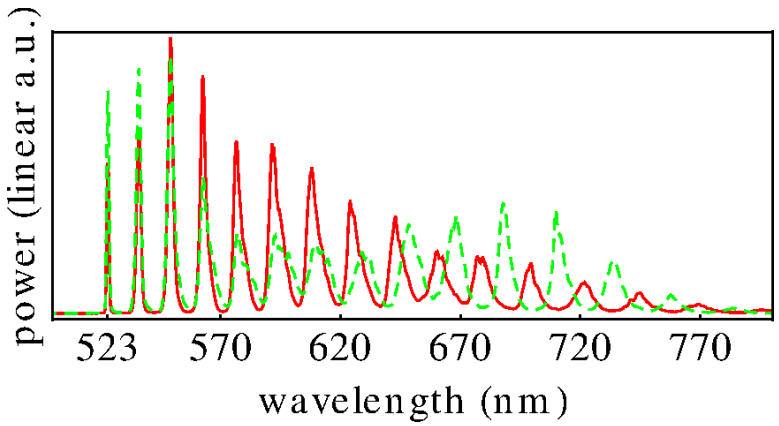

Figure 3.4: SRS spectra measured before (red solid line) and after (dashed green line) a slight offset of the pump beam from the fiber center. Shift of Raman peaks is caused by different FWM conditions caused by excitation of different fiber modes.

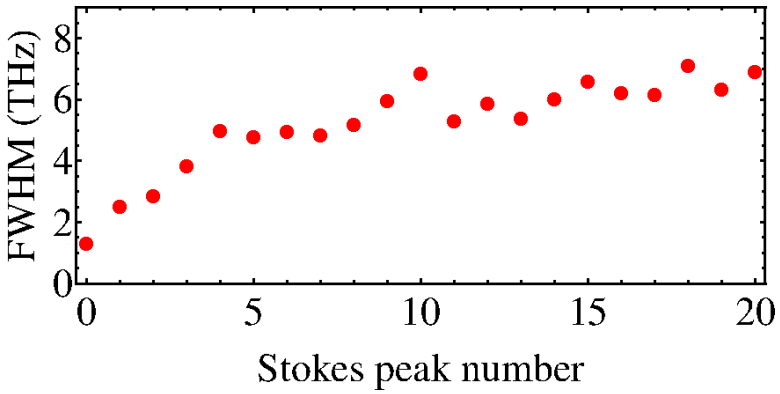

Figure 3.5: The FWHM spectral width of the Raman peaks from Figs. 3.1(a) and 3.3 are plotted as a function of the Stokes peak number. The Stokes peak numbers 0 and 1 correspond to the pump and the first order Raman peak, respectively.

Raman peak, separated by about 50 THz from the pump frequency, which is also consistent with the location of a FWM peak in Fig. 3.3. Also it have been observed that the shift is reversed if the input pump beam is aligned back with the center of the fiber core. Similar observations of the effect of the FWM processes on shifting the SRS spectrum have been reported by Sharma et al. [28]; they have shown that the cascaded Raman peaks can shift depending on which modes are excited by the pump laser.

In Fig. 3.5, the spectral width (full width at half maximum or FWHM) of the Raman

peaks from Figs. 3.1(a) and 3.3 plotted as a function of the Stokes peak number. The numbers 0 and 1 correspond to the pump and the first order Raman peak, respectively. Ref. [30] predicted that spectral width of each Raman peak is nearly twice that of the preceding order because of the broad bandwidth of the Raman gain in fused silica. The measured FWHM spectral widths of the pump and the first order Raman peak are 1.30 THz and 2.51 THz, respectively. According to Refs. [29,30], the spectral bandwidth of the Raman peak under certain conditions is nearly twice that of the pump. However, their analysis makes the undepleted-pump approximation and assumes an unchirped Gaussian profile for the pump pulse, neither of which apply to our experiment. Moreover, the noisy nature of the SRS peaks makes the analysis of Refs. [29, 30] even less applicable to the spectrum of higher-order Raman peaks. In our case, the bandwidths of higher-order Raman peaks show an increasing trend as a function of their Stokes peak numbers.

3.3 Spatial Beam Profiles and Beam Cleanup in SRS Generation

In continue with experiment the transverse intensity profile of the output beam have been measured by a CCD camera using several bandpass color filters with a FWHM spectral bandwidth of about 10 nm. The results are shown in Fig. 3.6. The profile in Fig. 3.6(a) is measured without a color filter, and the interference of multiple modes can be clearly observed as a speckle pattern. When a color filter centered at 610 nm is placed in front of the beam Fig. 3.6(b), a narrow round spot that appears to correspond to the spatial profile of the fundamental LG_{00} mode of used GIMF have been observed. It should be noteed that LG stands for Laguerre-Gaussian which are the eigenmodes of

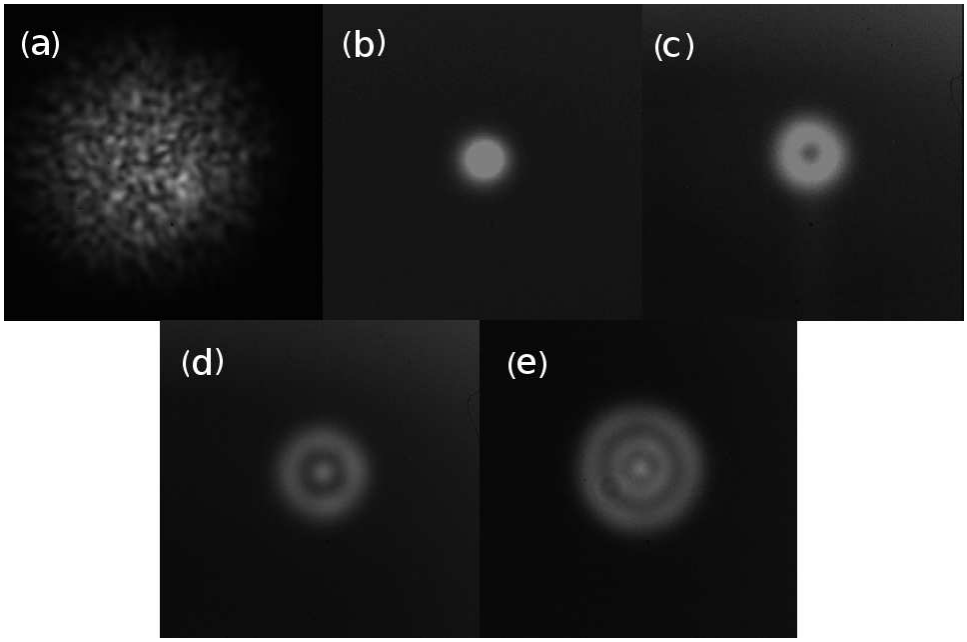

Figure 3.6: Measured spatial profiles using a CCD-based beam profiler. Image (a) is measured with no filters. The other 4 images are obtained using color filters centered at (b) 610 nm, (c) 700 nm, (d) 770 nm, and (e) 890 nm.

the GIMF under the weak-guidance approximation. The LG_{nm} modes can be related to the familiar notation of the $LP_{m,n+1}$ modes commonly used for step-index fibers. A donut-shape spot Fig. 3.6(c) is observed when a color filter centered at 700 nm is placed in front of the beam; the shape and the size of the beam makes it believe that it corresponds to the LG_{01} mode of fiber. Actually in practice, the two fold degeneracy of the LG_{01} mode is slightly broken to orthogonal double-lobed spatial profiles of Hermite-Gaussian modes [31] due to birefringence (similar to the two polarization of the LP_{01} modes). The donut shape in the measurement arises when both double-lobed spatial profiles are present simultaneously, primarily due to the large bandwidth (10 nm) of the color filter used for imaging the modes resulting from the incoherent combination of the orthogonal double-lobed spatial profiles.

Spatial beam profiles corresponding to higher-order fiber modes were also seen in the experiment. As two examples, images (d) and (e) of Fig. 3.6 show profiles correspond-

ing to the LG_{10} and LG_{20} modes. They were obtained by using optical filters with a 10-nm passband centered at 770 nm and 890 nm wavelengths, respectively. The most notable feature needs to be stressed is that a GIMF can be used as a device that not only shifts the pump wavelength toward the red side through SRS but also performs the beam cleanup owing to the fact that different-order Raman peaks generally propagate in different modes of the fiber. The main reason for the Raman beam cleanup is that the lower order modes generally have a larger Raman gain because of their greater overlap with the higher concentration of GeO_2 near the center of the GIMF core [21]. A detailed analysis of SRS-induced beam cleanup in graded-index multimode optical fibers can be found in Ref. [32]. Chiang reported similar results for higher order SRS combs in a 30-m-long fiber [33]. However, only LP_{01} mode (corresponding to LG_{00} mode here) was observed for a 1-km-long fiber. In our experiments, higher-order modes even for a 1-km-long fiber, have been observed and beam cleanup was not at the same level reported in Ref. [33].

3.4 Conclusion

In conclusion, we have used a standard, telecommunication-grade, graded-index multimode fiber for SRS generation by pumping it at 523 nm with 8-ns pulses. We observe multiple cascaded Raman peaks extending up to 1300 nm. Beyond that wavelength, the nature of dispersion changes from normal to anomalous because our fiber has its zero-dispersion wavelength near 1320 nm. At higher pump powers, in addition to the multiple cascaded Raman peaks, we observe a single broadband spectral peak, extending from 1350 to 1750 nm. Its origin appears to be related to the formation of solitons through modulation instability, intrapulse raman scattering, as well as collision-based spectral broadening. Such features have been observed in the past for single-mode

fibers or few-mode step-index fibers (see, e.g., Mussot et al. [34]). Our experiments show that a supercontinuum can also form in a highly multimode telecommunication-grade, graded-index multimode fiber. The multimode nature of the fiber can also be useful from a practical standpoint. For example, we observed that different spectral peaks have spatial patterns that correspond to different fiber modes. This feature can be useful for beam cleanup. Future efforts will focus on extending the spectrum to the infrared region and on stabilizing the frequency and power of individual comb lines for practical applications.

Bibliography

[1] A. C. S. Van Heel, "A New Method of transporting Optical Images without Aberrations", Nature **173**, 39 (1954)

[2] F. P. Kapron, D. B. Keck, R. D. Maurer, "Radiation Losses in Glass Optical Waveguids", Appl. Phys. Lett. **17**, 423 (1970)

[3] R. G. Smith, "Optical Power Handling Capacity of Low Loss Optical Fibers as Determined by Stimulated Raman and Brillouin Scattering," Appl. Opt. **11**, 2489 (1972)

[4] R. H. Stolen, "Nonlinearity in fiber transmission", Proc. IEEE 68, 1232 (1980).

[5] Essiambre, R.; Mestre, M.A.; Ryf, R.; Gnauck, A.H.; Tkach, R.W.; Chraplyvy, A.R.; Yi Sun; Xinli Jiang; Lingle, R., "Experimental Investigation of Inter-Modal Four-Wave Mixing in Few-Mode Fibers," Photonics Technology Letters, IEEE **25**, 539 (2013)

[6] A. Mafi, "Pulse Propagation in a Short Nonlinear Multimode Graded-Index Multimode Optical Fiber", J. Lightwave Technol. **30**, 2803 (2012).

[7] G. P. Agrawal, *Nonlinear Fiber Optics*, 5th ed. (Academic Press, 2012).

[8] R.H. Stolen; John E. Bjorkholm, "Parametric amplification and frequency conversion in optical fibers," Quantum Electronics, IEEE Journal of , **18**, 1062 (1982)

[9] C. Lin; M.A. Bosch, "Large-Stokes-shift Stimulated Four-photon-mixing in Optical Fibers", Applied Physics Letters **38**, 479 (1981)

[10] Q. Lin, F. Yaman, and G. P. Agrawal,"Photon-pair generation in optical fibers through four-wave mixing: Role of Raman scattering and pump polarization",Phys. Rev. A **75**, 023803 (2007)

[11] R. H. Stolen, "Phase-matched-stimulated four-photon mixing in silica-fiber waveguides," Quantum Electronics, IEEE Journal of , **11**, 100 (1975)

[12] P. Franken, A. E. Hill, C. W. Peters, and G. Weinrich, "Generation of Optical Harmonics" Phys. Rev. Lett. **7**, 118 (1961).

[13] R. H. Stolen, E. P. Ippen, and A. R. Tynes, "Raman Oscillation in Glass Optical Waveguide", Appl. Phys. Lett. **20**, 62 (1972).

[14] R. H. Stolen, J. E. Bjorkholm, and A. Ashkin, "Phase-matched three-wave mixing in silica fiber optical waveguides", Appl. Phys. Lett. **24**, 308 (1974).

[15] L. G. Cohen and C. Lin, "Pulse delay measurements in the zero-material-dispersion region for germanium- and phosphorus-doped silica fibres" IEEE J. Quantum Electron. **14**, 855 (1978).

[16] G. Rosman, "High-Order Comb Spectrum from Stimulated Raman-Scattering in a Silica-Core Fiber" Opt. Quantum Electron. **14**, 92 (1982).

[17] V. V. Grigoryants, V. I. Smirnov, and Y. K. Chamorovskii, "Generation of wide-band optical continuum in fiber waveguides", Sov. J. Quantum Electron. **12** 841 (1982).

[18] F. Couny, F. Benabid, P. J. Roberts, P. S. Light, M. G. Raymer, "Generation and Photonic Guidance of Multi-Octave Optical-Frequency Combs", Science **318** 1118 (2007).

[19] H. Pourbeyram; G. P. Agrawal, ; A. Mafi, "Stimulated Raman scattering cascade spanning the wavelength range of 523 to 1750 nm using a graded-index multimode optical fiber," Appl. Phys. Lett. **102**, 201107 (2013)

[20] J. Cheng, M. E. V. Pedersen, K. Charan, K. Wang, C. Xu, L. Gruner-Nielsen, and D. Jakobsen, "Intermodal Four-wave Mixing in a Higher-order-mode Fiber", Appl. Phys. Lett. **101**, 161106 (2012).

[21] A. Polley and S. E. Ralph, "Raman amplification in multi-mode fiber", IEEE Photon. Tech. Lett. **19**, 218 (2007).

[22] E. Golovchenko, P. V. Mamyshev, A. N. Pilipetskii, E. M. Dianov, "Mutual influence of the parametric effects and stimulated Raman scattering in optical fibers", IEEE J. Quantum Electron. **26**, 1815 (1990).

[23] F. Vanholsbeeck, P. Emplit, and S. Coen, "Complete experimental characterization of the influence of parametric four-wave mixing on stimulated Raman gain," Opt. Lett. **28**, 1960 (2003).

[24] B. H. Chapman, S. V. Popov, R. Taylor, "Continuous Wave Supercontinuum Generation Through Pumping in the Normal Dispersion Region for Spectral Flatness", IEEE Photon. Tech. Lett. **24** 1325 (2012).

[25] J. M. Dudley and J. R. Taylor, *Supercontinuum Generation in Optical Fibers*, 1st ed. (Cambridge University Press, 2010).

[26] F. Vanholsbeeck, S. Coen, P. Emplit, C. Martinelli, and T. Sylvestre, "Cascaded Raman generation in optical fibers: influence of chromatic dispersion and Rayleigh backscattering", Opt. Lett. **29**, 998 (2004).

[27] T. Sylvestre, H. Maillotte, E. Lantz, and P. Tchofo Dinda, "Raman-assisted parametric frequency conversion in a normally dispersive single-mode fiber," Opt. Lett. **24**, 1561 (1999).

[28] A. Sharma, M. Dokhanian, Z. Wu, A. Williams, and P. Venkateswarlu, "Four-photon-mixing-mediated stimulated Raman scattering in a multimode optical fiber", Opt. Lett. **19**, 1122 (1994).

[29] J. I. Gersten, R. R. Alfano, and M. Belic, "Combined stimulated Raman scattering and continuum self-phase modulations", Phys. Rev. A **21**, 1222 (1980).

[30] I. Ilev, H. Kumagai, K. Toyoda, and I. Koprinkov, "Highly efficient wideband continuum generation in a single-mode optical fiber by powerful broadband laser pumping", Appl. Opt. **35**, 2548 (1996).

[31] M. B. Shemirani, W. Mao, R. A. Panicker, and J. M. Kahn, "Principal modes in graded-index multimode fiber in presence of spatial-and polarization-mode coupling", J. Lightwave Technol. **27** 1248 (2009).

[32] N. B. Terry, T. G. Alley, and T. H. Russell, "An explanation of SRS beam cleanup in graded-index fibers and the absence of SRS beam cleanup in step-index fibers", Opt. Express **15**, 17509 (2007).

[33] K. S. Chiang, "Stimulated Raman scattering in a multimode optical fiber: evolution of modes in Stokes waves", Opt. Lett. **17**, 352 (1992).

[34] A. Mussot, T. Sylvestre, L. Provino, and H. Maillotte, "Generation of a broadband single-mode supercontinuum in a conventional dispersion-shifted fiber by use of a subnanosecond microchiplaser", Opt. Lett. **28**, 1820 (2003).